IOP Publishing Phys. Med. Biol. 65 (2020) 08NT02 https://doi.org/10.1088/1361-6560/ab8109

Physics in Medicine & Biology

IPEM Institute of Physics and Engineering in Medicine

NOTE

Towards customizable thin-panel low-Z detector arrays: electrode design for increased spatial resolution ion chamber arrays

Steffen Albert[1,2,3], **Davide Brivio**[1], **Saad Aldelaijan**[1], **Erno Sajo**[3], **Jürgen Hesser**[2] and **Piotr Zygmanski**

[1] Brigham and Women's Hospital, Harvard Medical School, Boston, MA, United States of America
[2] Heidelberg University, Heidelberg, Germany
[3] University of Massachusetts Lowell, MA, United States of America

E-mail: pzygmanski@bwh.harvard.edu

RECEIVED
23 September 2019

REVISED
12 March 2020

ACCEPTED FOR PUBLICATION
18 March 2020

PUBLISHED
23 April 2020

Keywords: ionization chamber, 3D printing, detector array, x-ray dosimetry, polarity, quality assurance, linac, IMRT

Abstract

The purpose of the present development is to employ 3D printing to prototype an ion chamber array with a scalable design potentially allowing increased spatial resolution and a larger active area. An additional goal is to design and fabricate a custom size thin-panel detector array with low-Z components. As a proof of principle demonstration, a medium size detector array with 30 × 30 air-vented ion chambers was 3D-printed using PLA as frame for the electrodes. The active-area is 122 mm × 120 mm with 4 × 4 mm^2 spatial resolution. External electrodes are cylindrical and made from conductive PLA. Internal electrodes are made from microwire. The array is symmetric with respect to the central plane and its thickness is 10 mm including build-up/-down plates of 2.5 mm thickness. Data acquisition is realized by biasing only selected chamber rows and reading only 30 chambers at a time. To test the device for potential clinical applications, 1D dose profiles and 2D dose maps with various square and irregular fields were measured. The overall agreement with the reference doses (film and treatment planning system) was satisfactory, but the measured dose differs in the penumbra region and in the field size dependence. Both of these features are related to the thin walls between neighboring ion chambers and different lateral phantom scatter in the detector panel vs homogeneous material. We demonstrated feasibility of radiation detector arrays with minimal number of readout channels and low-cost electronics. The acquisition scheme based on selected row or column 'activation' by bias voltage is not practical for 2D dosimetry but it allows for rapid turn-around when testing of custom arrays with the aid of multiple 1D dose profiles. Future progress in this area includes overcoming the limitations due high chamber packing ratio, which leads to the lateral scattering effects.

1. Introduction

Developing 2D radiation detector arrays with many sensing elements faces several challenges including relatively large amount of wiring in the backbone of the detector panel and large number of data acquisition channels, which complicates design and fabrication, increases the costs and leads to dosimetric artifacts due to the use of high-Z materials (Zygmanski *et al* 2014, Chandraraj *et al* 2011, Brivio *et al* 2019, Albert *et al* 2019). To circumvent these problems, a method employing selective 'activation' of a smaller number of detector elements was explored, effectively giving rise to 2D dosimetry within a thin-panel tissue-equivalent array (figure 1). Activation implies the selective utilization of high bias voltage applied to some chambers and not to the others, or applying different polarity high bias voltages as is explained in the Methods section.

Commercial radiation detector arrays used in radiotherapy comprise diode or ion chamber arrays embedded in flat panels or cylindrical shells (Macdonald *et al* 1992, Bedford *et al* 2009, Wolfsberger *et al* 2010, Aristophanous *et al* 2016). With many detector elements the detector backbone contains a relatively large amount of medium- to high-Z wiring with leads connected to many data acquisition channels. The

© 2020 Institute of Physics and Engineering in Medicine

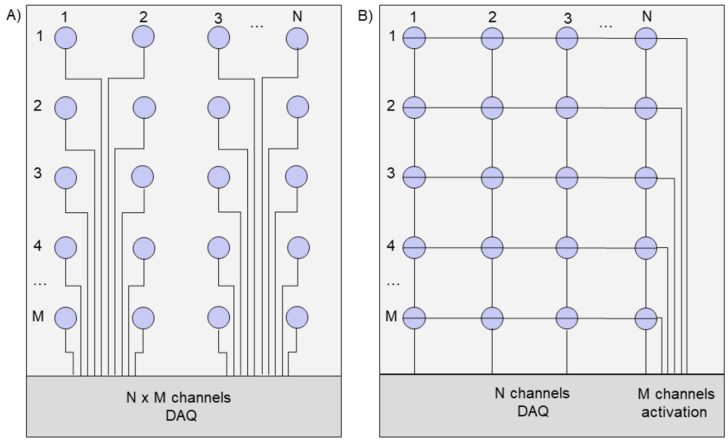

Figure 1. (A) In traditional 2D arrays, each of the NM detector elements is independently wired and connected to one data acquisition channel. Thus, the total number of channels is N × M and is typically on the order of about 1000. This also means that N × M wires or leads are required in the backbone of the detector panel. (B) In the proposed detector the design is simplified with significantly reduced number of data acquisition channels and wiring down to (M + N). In the example, individual detector elements are selectively activated. 2D dose maps are acquired by iterative acquisition of 1D dose profiles one at a time (N dose data points × M times).

number of detector elements is typically limited to about 1000 (1069 for Delta4 from ScandiDos, 1386 in the ArcCheck from SunNuclear, 1020 in Matrixx from IBA and 977–1405 in Octavius from PTW), which results in spatial resolution from about 5 mm in the central region to 10 mm away from the center. Integration of significantly more detector elements into the present detector panel design would be difficult and costly due to electro-mechanical design and both radiation and electrical effects in compact detector geometries. New more efficient approaches must therefore be explored to allow further progress towards higher definition thin-panel and, ideally, tissue-equivalent arrays.

Our long-term goal is to develop a low-cost methodology for the fabrication of thin-panel (5 mm or less) low-Z (and possibly tissue-equivalent) custom detector arrays for radiation dosimetry. Such arrays could be integrated into specialized phantoms (Brivio *et al* 2019) or the linac head. The present work aims at demonstrating a new detector array design with significantly reduced wiring and smaller number of data acquisition channels compared to the number of detector elements in the array. Thanks to the new design, the fabrication of a thin-panel detector array with low-Z materials is possible in the clinical environment. The new detector design includes unique electrode and chamber geometry and array design that is scalable to potentially smaller chamber sizes and high chamber packing as well as larger detector area size compared to the past detector arrays prototyped employing 3D printing (Albert *et al* 2019).

To demonstrate the new detector design low-cost FDM 3D printing is employed using insulating and conductive filament materials (Albert *et al* 2019). In this proof of principle demonstration, air-vented ionization chambers are chosen as detector elements, which practically constrained the spatial resolution to about 4 × 4 mm^2 and detector volume to 28 mm^3 but allowed straightforward and rapid prototyping of the detector panel with all the elements including the conducting leads and sockets for cables of the data acquisition system. In contrast to (Albert *et al* 2019), the chamber size and center-to-center distance was decreased, the number of detector elements increased and the design of the detector was changed to eliminate any gaps with a low electric field-strength. This made it possible to record doses with better spatial resolution and decreased the electric field degradation within the chamber and within array volume.

2. Methods and materials

Several prototypes of the detector were designed, and 3D printed using an FDM printer (LulzBot TAZ 6) (Albert *et al* 2019). Only the latest version of the array with 900 cylindrical, air-vented ionization chambers that are arranged in a 30 by 30 grid (visible in figure 2) is reported here (Chandraraj *et al* 2011). Their inner dimensions are 3 mm in diameter and 4 mm in length. The external electrodes are made of conductive PLA (cPLA, Electrically Conductive Composite PLA from Proto-Pasta, made by adding carbon black flakes to PLA) rods (4 mm × 5 mm × 130 mm) with cylindrical holes every 4 mm. Because the internal electrodes should have small cross sections we tested materials possessing different electro-mechanical properties: 3D printed cPLA (1 mm × 0.4 mm), carbon fiber (CF) yarn (120 μm diameter) and metal alloy microwire (130 μm diameter).

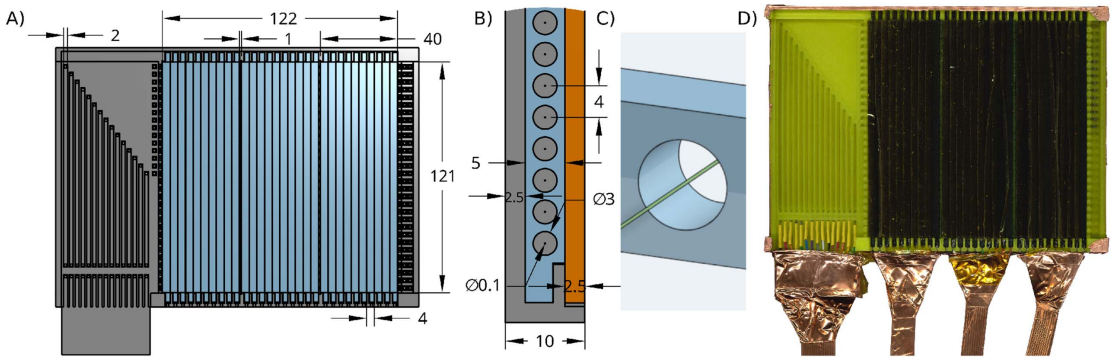

Figure 2. (A) CAD drawing of the bottom half of the detector. All dimensions are in mm. The blue rods form the external electrodes. The external electrodes are held in place by the PLA fixture and are electrically isolated by Kapton foils. Every 10 channels, there is a 1 mm wall to support the central electrodes and prevent them from sagging. (B) Cross section of one external electrode. The external electrode is 5 mm thick and is inserted into the bottom plate (gray) and covered by the top plate (orange), which are both 2.5 mm thick, bringing to total thickness to 10 mm. There are cylindrical holes with 3 mm diameter which form the ion chambers. They are separated from each other by 1 mm walls. The inner electrode runs through the center of the chamber as seen in the Volume rendering (C). Only one inner and one external electrode are shown. (D) The (partially) assembled detector. On the left are M = 30 wires connected to internal electrodes, which are horizontal, and which are used for activation of chambers. Another similar plate is added on top to carry the other half of the wires. Each external electrode is connected to one wire and 10 of these wires are combined into one cable, which is connected to the data acquisition system.

The internal electrodes are held in place by a fixture made from non-conductive PLA outside the active area of the detector. The external electrodes are separated by a thin (70 μm) layer of Kapton foil for electrical insulation with a hole at each chamber to let the inner electrode pass through the foil.

This results in a 4 mm center-to-center distance in the plane of the detector. The total thickness of the detector panel is 10 mm including 2.5 mm thick build-up/down slabs on both sides. The thickness could be reduced to 5–7 mm by printing thinner build-up/build-down slabs. Every 10 chambers, there is a 1 mm wall between the external electrodes to hold the internal electrode in place, so the active area measures 122 mm $\times$ 120 mm including the two internal support walls.

The internal electrodes are used to apply the bias voltage. The bias voltage is controlled using an inexpensive custom PCB with 64 channels, which can switch each channel between a high voltage (up to $\pm$ 200 V) and a low voltage (up to $\pm$ 100 mV) and is connected to the computer using a microcontroller. The switching time of the voltage controller is 50 ms. Data acquisition utilizes 128-Channel, 24-Bit Current-to-Digital Converter ADAS1134 (Analog Devices).

The voltage is used to activate and deactivate the individual sensor elements by biasing them with high voltage or low voltage. High voltage is applied to the internal electrode of the rows that should be activated and low voltage to the remaining internal electrodes. In the present prototype, when switching the internal electrodes to ground, a small voltage remains due to leakage on the PCB and work function differences between central and external electrodes. The contact potential between the central and external electrode can be avoided by using the same electrode materials as discussed in the Discussion section. To circumvent the small voltage biases and leakage, a workaround measurement was designed with all internal electrodes at high voltage and then the active rows are switched to negative high voltage and the difference in the signal is measured.

All measurements were carried out using a Varian Truebeam linac as radiation source, with the detector at the isocenter of the linac. Phantom was made of two slabs of solid water of 4.5 cm, and 5 cm thickness used as buildup and backscatter materials. The source to surface distance was 95 cm.

To test the array in clinical beams square and irregular MLC fields were used. All fields were measured using 100 MU of radiation at a dose rate of 600 MU min^{-1} and an energy of 6 MV. 1D dose profiles were acquired in sequence by applying a constant voltage of 50 V to all the internal electrodes except one selected electrode, which was biased at -184 V. By repeating this process for all the internal electrodes, a 2D dose distribution map was generated. The ICs were calibrated using a 15 cm $\times$ 15 cm open field. Dose distribution maps measured with the sensor array are compared to doses measured using gafchromic film as well as to doses computed by Treatment Planning System (TPS) (Eclipse, Varian). Gafchromic film dosimetry was performed for the test fields as described in reference (Aldelaijan *et al* 2019).

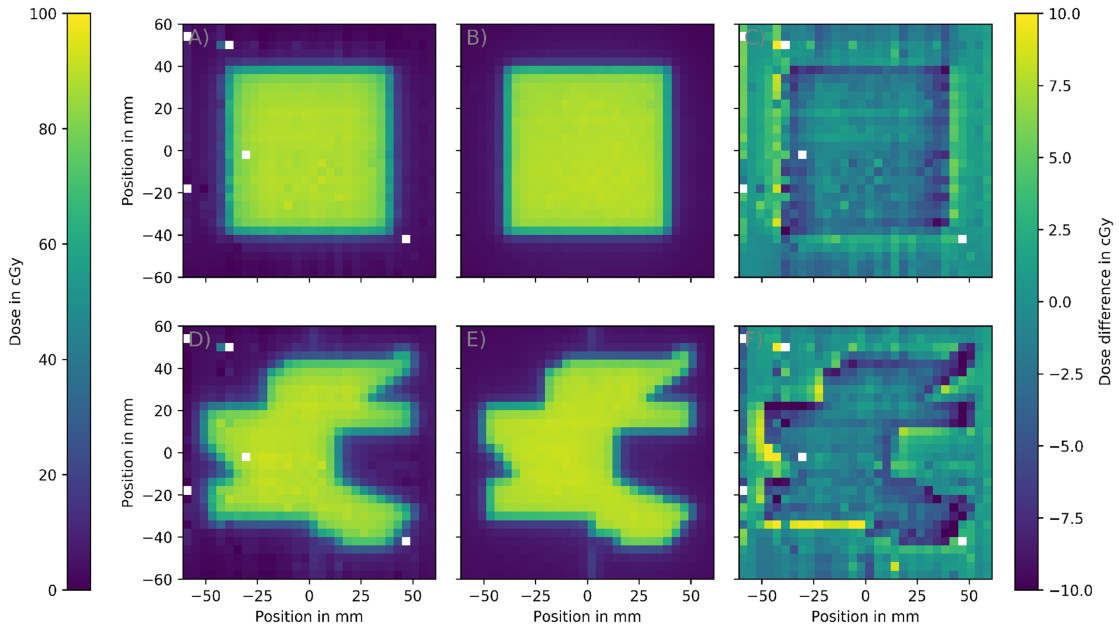

Figure 3. Multiple dose profiles. (A) shows selected profiles along the columns located at x = − 46 mm, x = 2 mm and x = 38 mm from the same measurement as in figure 3. In (B) multiple square fields are visible, which were recorded along one of the central rows of the detector. The dotted lines show the dose predicted by the treatment planning system and the dashed line the dose measured with gafchromic film (Aldelaijan *et al* 2019).

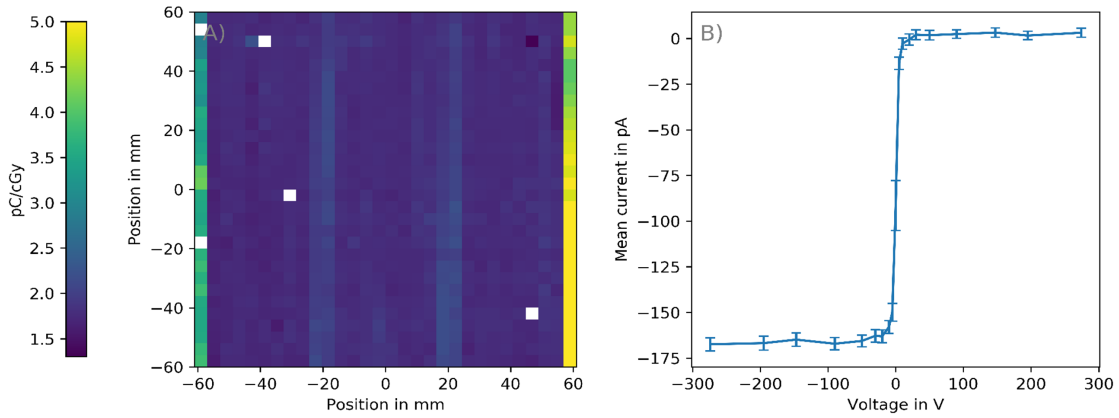

Figure 4. Different properties of the detector. (A) shows the charge per dose for each pixel after calibration. It is visible that the first and last columns collect charges from outside, which leads to a higher signal. At position −20 mm and 20 mm are 1 mm thick walls holding the internal electrodes, which also leads to a higher signal, due to a small air gap present there. The IV curve for the mean of all working pixels except the one neighboring a gap is visible in (B).

3. Results

Dose distribution maps measured with our sensor array vs the reference data (gafchromic film and doses computed by TPS) are seen in figures 3 and 4. The overall relative difference compared to the reference data for both of the images seen in figure 3 is 3% in high dose regions (>10 cGy), which account for around half of all pixels. This shows satisfactory agreement for the prototype considering small chamber volumes and design/fabrication restrictions imposed by 3D printing technique (Albert 2019). The highest absolute differences occur in regions with high dose gradients. In the low dose regions, the relative difference is 50% while the absolute difference is only 1.5 cGy.

The first and last columns have a higher signal due to being able to collect charges from small gaps outside the active area as visible in figure 5, which could be removed in a future design. The signal is also stronger in the channels next to the PLA walls that suspend the central electrode. All the other ICs have a similar dose per charge, with a mean standard deviation of about 3%. Some ion chambers had higher leakage due to contamination of chamber with conductive material during fabrication and were not suitable for dosimetry. Those are visible as white pixels in figure 3.

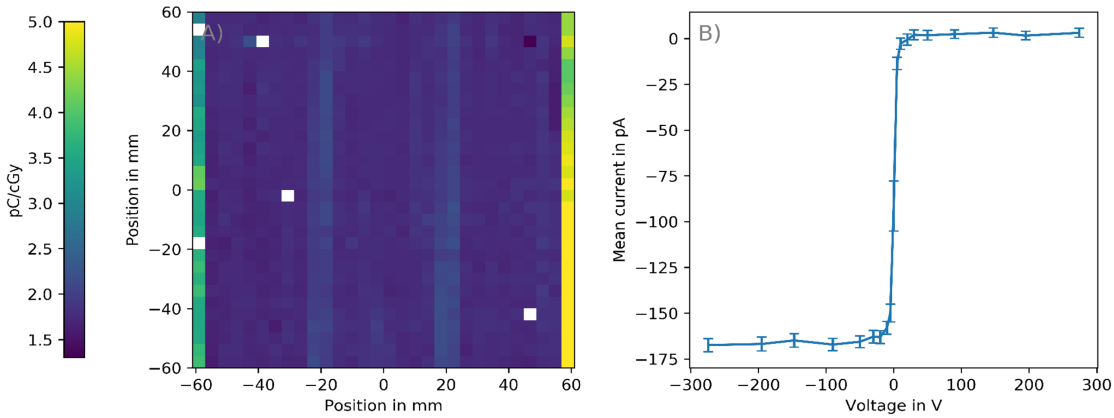

Figure 5. 2D Dose profiles for two different fields. The measured dose can be seen in the first column (A) and (D) and the two images in the second column (B) and (E) show the dose measured using gafchromic film (Aldelaijan *et al* 2019). These 4 images are using the left color scale. The absolute difference can be seen in the last column (C) and (F), which uses the right color scale. The film dose is averaged over a 4 mm by 4 mm area to make it comparable to the resolution of the detector. Images (A) and (C) show the dose for an 8 cm by 8 cm that was created using the jaws. For (B) and (D), an MLC pattern was used to create a field with more interesting features. Both fields were measured using 100 MU of radiation at a dose rate of 600 MU min^{-1} and an energy of 6 MV. The unusable chambers appear white.

There was no measurable dose rate dependence. The dose rate is only varied by changing the time between linac pulses, so the instantaneous dose rate could not be changed without changing source to distance, which would change the head scatter and phantom scatter. The IV-curve in figure 5 shows, that saturation is reached quickly and the voltages that were used are well in the saturation region. Differences between positive and negative polarity could not be measured in this setup.

After the onset of radiation, the current stabilizes quickly and the rise cannot be observed with an integration time of 2.5 ms. Only the channels on the outside and next to the PLA walls take 1–3 s to reach a constant current.

Dose profiles for square fields of various sizes are seen in figure 4(B). The overall agreement is 3% in high dose regions, but compared to the dose measured using gafchromic film (Aldelaijan *et al* 2019). The differences are larger in the penumbra region and for smaller field sizes. The reason for this discrepancy is discussed in the following section.

4. Discussion and conclusion

Activation of selected detector elements in the detector array allows non-standard and simplified wiring of the detector and substantial reduction of the data acquisition channels (from $N \times M = 30 \times 30 = 900$ to $N = M = 30$). Therefore, off-the-shelf data acquisition electronics with up to 128 femto-ampere ADC channels can be readily used for the total of 900 ion chambers. This in turn facilitates custom design and fabrication of a thin-plate (down to 5 mm) low-Z detector array with a symmetric design of the active area with respect to the central plane of the detector. The detector plate thickness is essentially limited by the height of the ion chambers. The detector array was fabricated using low-cost FDM 3D printing with electrically insulating and conductive filaments (ABS, PLA, cPLA), which grants fast prototyping of several versions of the array with slightly different designs and central electrode material.

In our initial intention, we aimed using low-Z polymer materials for all the elements of the detector panel, however, 3D printing of the central electrode with about 1 mm × 0.4 mm cross section made of conductive PLA was not favorable for ion collection (electric field distortions compared to cylindrical central electrode geometry) and spatial resolution of the chambers (related to the reduction in chamber volume). For these reasons, central electrodes with a smaller diameter were tested using Carbon Fiber (CF) yarn and metal alloy microwire. Unfortunately, while CF yarn was initially very appealing it was found not usable in practice due to the presence of micro-fibers, which split off from the main stem of the yarn in all directions and caused electrical shorts in many locations. These microfiber yarns contaminated some chambers and caused higher leakage and made them in practice not suitable for dosimetry (white spots in figures 3(A) and (B).

An alternative solution to the CF is Conductive Carbon Nanotube (CNT) yarn, which is smoother on the surface (and significantly more expensive). However, in this demonstration, we decided to use only low-cost materials. On the other hand, metal microwire, while being the easiest in fabrication and use has larger Z and different work function than conductive PLA. The Work function difference leads to about 400 mV internal

contact potential, which partially activates all the channels when 0 V are applied. For this reason, in our activation scheme we selected +50 V/−200 V (in)activation voltages rather than 0 V/200 V.

A second motivation for using this voltage switching scheme is the presence of a memory effect due to dielectric polarization of PLA and ABS dielectric materials. Using non-zero voltage in the saturation region for the 'inactive' channels reduces effects due to dielectric polarization of PLA observable at 0 V biases. Dielectric polarization must be distinguished from ion chamber polarity effect. Dielectric polarization and relaxation phenomena are due to multiple factors including external electric field, triboelectric effects, temperature, and radiation effects and can be utilized in radiation detection (Ryner 1990, Berghofer *et al* 2003, Denman *et al* 2004). However, in the context of our ion chamber array these effects lead to undesired effects such as non-zero signal for 0 V external bias, or stabilization problem with some chambers.

In a future design, the central electrode must be made of smooth and cylindrical lower-Z material (e.g. CNT yarn) and external electrode should be coated with low-Z conductive polymers to improve the screening of dielectric dipoles in the polymers and guarantee the elimination of the aforementioned undesirable effects. In addition, new conductive 3D printing materials should be explored to increase their conduction and decrease dielectric polarization effects.

Another limitation of the present ion chamber-based array with thin conductive PLA chamber walls is relatively smaller lateral scatter (compared to water) in the plane of the 10 mm thick detector panel. This is especially visible in the square field profiles (figure 4(B)). The discrepancy is higher for smaller fields due to the lack of lateral charged particle equilibrium within the detector panel, whose effective density is smaller than solid material. Monte Carlo simulations in similar geometries show that the differences seen in figure 4 are due to radiation effects related the lateral scatter in water alone vs high definition air-vented chamber array. A potential solution to this problem is to use more precise dose computations that account for the presence of air vented ion chambers or the introduction of thicker walls between the chambers. The latter was not attempted because that would restrict the spatial resolution of the array. This also proves the limitation of air vented ion chamber arrays related to spatial resolution.

The limiting factors of the present prototype detector array that impact spatial resolution are volume of the chambers and center-to-center distances. Air-vented ion chambers cannot have much smaller volume than in the present version (28 mm^3), because of signal-to-noise ratio for clinically realistic x-ray fluxes. The noise without radiation was 2.3 pA, which is about 1% of the current per chamber at 600 MU min^{-1} using a flat field. A potential solution is to use ionic liquids instead of air to generate charge carriers (Van Herk 1991, Ehler *et al* 2014). By using ionic liquids, the chamber geometry can be not only made smaller but also simpler. One could use parallel-plate geometry to limit the volume down to about 2.5 mm × 2.5 mm × 0.5 mm. Using liquid-filled ionization chambers would also remove the problem related to the lateral scatter of the air vented chamber array. Using solid state semiconductors would certainly allow even larger spatial resolution but would also pose new problems due to their intrinsic response, which depends on the quality of the semiconductor. And quality come at a high price especially for high density detector elements.

In conclusion, it was demonstrated that the selective activation of detector elements and 3D printing allow rapid prototyping of thin-plate low-Z detector arrays for radiotherapy linac QA or some specialized dosimetry tasks. The new electrode, chamber and array design is scalable to potentially smaller chamber sizes and even higher density and larger active area of the array, but it also poses new problems due to insufficient latter scattering in the plane of the detector, which impacts the beam properties at the edges of the field compared to 3D uniform water medium.

The main advantage of N × M arrays with N readout channel is relatively small number of data acquisition channels and possibility of using low cost of off-the-shelf multichannel electronics. Second, substantially decreased wiring leads to major redesign of the array and achieving a thin-plate composed of low-Z materials. Except for the proof or principle purposes, specific clinical applications of such arrays remain to be explored in the future. One of the possibilities is in monitoring of beam stability for which detector response might be different from absolute dosimetry with a point detector in water (Islam *et al* 2009). For instance, response of Integral Beam Monitor (IQM) by iRT or EPID by linac manufacturer can be used to monitor the beam, although their response is design and material dependent. However, with proper calibration one can determine several important quantities such as MLC positions or even 3D dose distribution by back-projecting of MLC apertures onto patient CT by mounting the detector directly at the linac head in front of the MLCs (Wong *et al* 2012, Alrowaili *et al* 2016).

Acknowledgment

We would like to acknowledge Rachel Trevillian for performing Mont Carlo simulations of the air vented ion chamber array.

ORCID iDs

Steffen Albert https://orcid.org/0000-0003-4424-750X
Davide Brivio https://orcid.org/0000-0002-4127-9955
Saad Aldelaijan https://orcid.org/0000-0002-9085-8988
Erno Sajo https://orcid.org/0000-0001-6802-0014
Jürgen Hesser https://orcid.org/0000-0002-4001-1164

References

Albert S 2019 Prototyping of thin water equivalent ionization chamber arrays with 3D printing *Unpublished Masters Thesis* (Heidelberg: Universität Heidelberg)

Aldelaijan S, Devic S, Papaconstadopoulos P, Bekerat H, Cormack R A, Seuntjens J and Buzurovic I M 2019 Dose–response linearization in radiochromic film dosimetry based on multichannel normalized pixel value with an integrated spectral correction for scanner response variations *Med. Phys.* **46** 5336–49

Alrowaili Z A, Lerch M L, Petasecca M, Carolan M G, Metcalfe P E and Rosenfeld A B 2016 Beam perturbation characteristics of a 2D transmission silicon diode array magic plate *J. Appl. Clin. Med. Phys.* **17** 85–98

Aristophanous M, Suh Y, Chi P C, Whittlesey L J, Laneave S and Martel M K 2016 Initial clinical experience with ArcCHECK for IMRT/VMAT QA *J. Appl. Clin. Med. Phys.* **17** 1–14

Bedford J L, Lee Y K, Wai P, South C P and Warrington A P 2009 Evaluation of the Delta4 phantom for IMRT and VMAT verification *Phys. Med. Biol.* **54** N167–76

Berghofer T *et al* 2003 Liquid ionization chambers for radiation therapy *2003 IEEE Nuclear Science Symp. Conf. Record (IEEE Cat. No. 03CH37515)* vol 3 (Piscataway, NJ: IEEE)

Brivio D, Naumann L, Albert S, Sajo E and Zygmanski P 2019 3D printing for rapid prototyping of low-Z/density ionization chamber arrays *Med. Phys.* **46** 5770–9

Chandraraj V, Stathakis S, Manickam R, Esquivel C, Supe S S and Papanikolaou N 2011 Comparison of four commercial devices for RapidArc and sliding window IMRT QA *J. Appl. Clin. Med. Phys.* **12** 338–49

Denman A R, Groves-Kirkby C J, Phillips P S, Crockett R G and Woolridge A 2004 Domestic radon monitoring with electrets – practical experiences of large-scale use *IRPA Conf.* (*Madrid, Spain*)

Ehler E D, Barney B M, Higgins P D and Dusenbery K E 2014 Patient specific 3D printed phantom for IMRT quality assurance *Phys. Med. Biol.* **59** 5763

Islam M K, Norrlinger B D, Smale J R, Heaton R K, Galbraith D, Fan C and Jaffray D A 2009 An integral quality monitoring system for real-time verification of intensity modulated radiation therapy *Med. Phys.* **36** 5420–8

Macdonald B A, Fallone B G and Ryner L N 1992 Feasibility study of an electric dosimetry technique *Phys. Med. Biol.* **37** 1825

Ryner L 1990 An electret dosimeter charged by radiation-induced ionizations in air *MSc Thesis* (Montreal: McGill University)

Van Herk M 1991 Physical aspects of a liquid-filled ionization chamber with pulsed polarizing voltage *Med. Phys.* **18** 692–702

Wolfsberger L D, Wagar M, Nitsch P, Bhagwat M S and Zygmanski P 2010 Angular dose dependence of Matrixx TM and its calibration *J. Appl. Clin. Med. Phys.* **11** 3057

Wong J H D, Fuduli I, Carolan M, Petasecca M, Lerch M L F, Perevertaylo V L and Rosenfeld A B 2012 Characterization of a novel two dimensional diode array the magic plate as a radiation detector for radiation therapy treatment *Med. Phys.* **39** 2544–58

Zygmanski P, Abkai C, Han Z, Shulevich Y, Menichelli D and Hesser J 2014 Low-cost flexible thin-film detector for medical dosimetry applications *J. Appl. Clin. Med. Phys.* **15** 4454